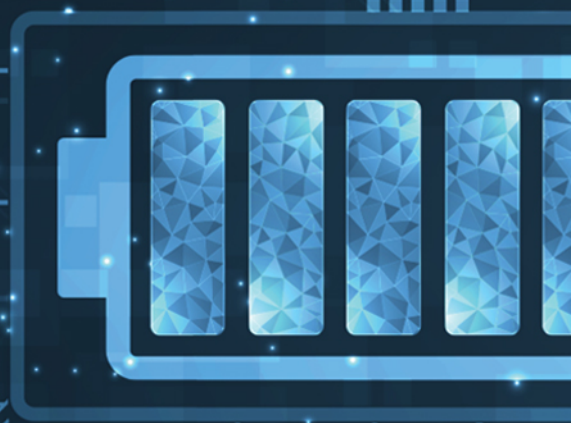


# ANALYTICAL SOLUTIONS TO DRIVE THE ENERGY REVOLUTION

Our comprehensive portfolio of analytical solutions for battery materials testing has the flexibility to support ongoing innovations and keep up with your laboratory's ever-changing requirements.

Carry out investigations to improve the performance, positivity, conductiveness and other properties of your battery parts such as cathode, anode, electrolyte, separators, membranes, and binders.

Providing the chemical and material analysis you need, we help you innovate in batteries for safety, performance, power, longevity, scale and weight.



Learn more at  
[www.perkinelmer.com/category/energy-storage](http://www.perkinelmer.com/category/energy-storage)

  
**PerkinElmer**<sup>®</sup>  
*For the Better*

# A Multiscale Flow Battery Modeling Approach Using Mass Transfer Coefficients

Amadeus Wolf,\* Emmanuel Baudrin, and Hermann Nirschl

A novel multiscale flow battery simulation approach is presented. Therefore, the mass transfer coefficient (MTC) is extracted from the 3D-resolved microscale simulations, transferred to the homogenized cell scale and compared to empirical formulations from literature. The models are parameterized with an organic system and experimentally validated on the microscale. It resolves the real geometry of the electrode microstructure obtained by experimental image reconstruction from microtomography. It accounts for flow, mass, and coupled charge transport using Butler–Volmer kinetics. It is suitable to study power density as a function of concentration, velocity, and discharge rate. The MTC is extracted under transfer-limiting operating conditions. Bulk and surface concentrations of active material and the reaction rate are used. The 2D homogenized cell-scale model considers half-cell single species transport and reduced order reaction. The extracted MTC is implemented as a function of state of charge (SOC) and velocity, distinctive for specific initial concentration and discharge rate. It is used to calculate the reaction rate for evolving species in the electrode and is investigated in a parameter study. The approach is compared to empirical formulations of the MTC based on velocity. It can be shown that the MTC is one order of magnitude higher and depends significantly on SOC.

concept of flow batteries is based on the spatial separation of electrolyte and electrode which results in the independent scalability of power and capacity.<sup>[2,3]</sup> This makes them applicable in a wide energy range of the grid infrastructure. Moreover, long operating life cycles, environmental friendliness, and nonflammability are further advantages toward predominant storage systems.<sup>[4,5]</sup> However, high capital costs and low energy density predominantly have been preventing a deep market penetration up to the present.<sup>[6]</sup>

A typical flow battery consists of two independent reservoirs holding separated electrolyte solutions and two porous electrodes separated by an ion transport membrane. During operation, the electrolytes are pumped through the electrochemical cell, where the redox reaction takes place at the surface of the porous electrodes. Subsequently, the charged or discharged electrolyte flows back into the reservoir.<sup>[7,8]</sup> The all-vanadium system is so far the most studied and developed flow battery

system, which convinces by the absence of material degradation and capacity fade.<sup>[9,10]</sup> However, it suffers from the comparatively high prices and enormous price fluctuations regarding the electrolyte,<sup>[11]</sup> and from the fact that vanadium is a critical raw material.<sup>[12]</sup> Recently, organic redox-active materials have emerged as a promising alternative to metal-based systems due to their low cost, structural designability, and the independence on metal mining.<sup>[13,14]</sup> For this reason, this contribution focuses on an electrolyte for aqueous organic redox flow batteries, namely 4-hydroxy-2,2,6,6-tetramethylpiperidin-1-oxyl (4-OH-TEMPO).<sup>[11,15]</sup>

Simulation methods are powerful tools for gaining insight into the multiphysical processes inside the battery and for predicting its performance for various operating conditions. They provide a substantial alternative to experimental investigations as these can be very challenging and costly in terms of raw materials, physical resources, and time. Modeling approaches for flow battery components and performance apply to a wide range of length scales. This contribution focuses on a detailed microscale model (MSM) and an upscale connection to a homogenized cell-scale model (HCSM).


Three-dimensional MSMs resolve the actual electrode geometry to gain insights of the micro-structural processes within the battery. The structure of the electrode is obtained by image processing and reconstructing, mostly using X-ray-computed

## 1. Introduction

Driven by the transformation of the energy system and the need to store fluctuating power generation from renewable energy sources, stationary storage systems become more and more important.<sup>[1]</sup> Flow batteries are promising candidates for balancing the demand and supply in the electrical grid and thus providing continuous and reliable power supply. The unique

A. Wolf, H. Nirschl  
Institute for Mechanical Process Engineering and Mechanics  
Karlsruhe Institute of Technology  
Strasse am Forum 8, 76131 Karlsruhe, Germany  
E-mail: amadeus.wolf@kit.edu

E. Baudrin  
Laboratoire de Réactivité et Chimie des Solides  
Université de Picardie Jules Verne  
Chemin du Thil - CS 52501 - 80025 Amiens Cedex 1, France

 The ORCID identification number(s) for the author(s) of this article can be found under <https://doi.org/10.1002/ente.202300175>.

© 2023 The Authors. Energy Technology published by Wiley-VCH GmbH. This is an open access article under the terms of the Creative Commons Attribution License, which permits use, distribution and reproduction in any medium, provided the original work is properly cited.

DOI: 10.1002/ente.202300175

micro-tomography (XCT).<sup>[16–18]</sup> The governing equations for fluid flow, species transport, and reaction are directly solved on the computational grid. Hence, MSMs provide spatially resolved characteristics of, e.g., velocity, concentration, current density, or overpotential depending on the complex structures of the electrode. In contrast, expensive imaging experiments and meshing processes make MSM a comparatively nontrivial endeavor. The resulting mesh consists of millions of computational cells and is thus reliant on high-performance cluster computing. Qiu et al.<sup>[16,19]</sup> developed the first MSM for a vanadium flow battery. The fluid flow was simulated using the lattice Boltzmann method (LBM) while the coupled species and charge transport were described using the finite volume method (FVM). Battery performance and reaction distribution under different operating conditions were investigated along with the varying morphology of the electrode. With this work, the basis was set for further MSM development in the flow battery context.<sup>[17,18,20,21]</sup>

Most of the flow battery modeling approaches to date have been concentrating on the volume-averaged or macroscopic calculation of transport processes within porous electrodes captured by using empirical relations, e.g., Darcy's law or Bruggeman relation.<sup>[22–26]</sup> Here, the electrode is assumed to be spatially uniform, while studies have shown that the models are not able to predict the partially in-homogeneous flow distribution observed experimentally within the electrode.<sup>[27]</sup> No detailed information about the electrode microstructure is required, and the reaction can be treated in simplified terms.<sup>[28,29]</sup> As a consequence, larger computational domains incorporating single or multicell applications as well as membrane transport can be simulated. 2D homogenized models are favored in cell optimization calculations<sup>[30]</sup> and promising for industrial applications<sup>[31]</sup> due to their reduced complexity and low computational cost. In contrast, the homogenization process entails an information loss which is generally compensated for by experimental or MSM information. For a more detailed roundup of flow battery modeling approaches on different scales, the reader is referred to recent extensive reviews on these fields.<sup>[32–36]</sup>

However, it is remarkable that few approaches of connecting the scales in flow battery modeling have been reported in the literature. Franco et al.<sup>[37]</sup> reviewed different concepts and approaches of multiscale modeling with a focus on lithium ion batteries. Recently, Bao et al.<sup>[38]</sup> coupled a flow battery 1D half-cell device model with a deep neural network model to optimize the time-varying inlet velocity of the electrolyte. The neural network was trained using pore-scale simulations. Tao et al.<sup>[39]</sup> reported a framework for modeling ion transport in porous material, combining molecular dynamics simulation at the nanopore level and continuum modeling for the pore network.

In general, efficient ways of passing information between different scale models are difficult to determine. This publication continues the research on multiscale modeling of flow batteries by introducing an approach for connecting a 3D-resolved MSM introduced in previous work<sup>[40]</sup> with a 2D HCSM. The work investigates flow battery performance using the MSM with reconstructed microstructure. Further, different flow directions are statistically investigated under different operating conditions. Finally, the connection of the different scale models is achieved

by the extraction of the mass transfer coefficient  $k_m$  from MSM and its transfer to the HCSM.

Generally, the mass transfer coefficient is derived from the principles of gas absorption<sup>[41]</sup> and characterizes the mass transfer resistance. It can be obtained using empirical correlations of the velocity<sup>[42–44]</sup> or the limiting current density.<sup>[45,46]</sup> You et al.<sup>[47]</sup> quantified the impact of velocity on the mass transfer coefficient in a Fe<sup>2+</sup>/Fe<sup>3+</sup> lab-scale flow battery. The resulting correlation was incorporated into a 2D numerical model, and voltage losses of experiment and simulation were compared. Milshtein et al.<sup>[48]</sup> developed a 1D flow battery model also using iron chloride to investigate the electrode polarization. With experimental fitting, mass transfer coefficients for different flow fields were extracted. A direct numerical simulation method to determine the effect of micro-structural anisotropy on the mass transfer coefficient was presented by Kok et al.<sup>[17]</sup> The LBM was applied on XCT-computed digital twins on three different fibrous electrode materials. Dimensionless correlations were determined with respect to the materials' permeability.

Several homogenized modeling approaches use the mass transfer coefficient to compensate the unknown surface concentration of active material on the electrode.<sup>[22,23]</sup> Since MSMs resolve the mass transfer between bulk and active surface, this relation is not prerequisite.<sup>[21,49]</sup> Accordingly, the coefficient is extracted from the MSM and implemented into the HCSM as a function of state of charge and velocity in this contribution. Furthermore, it is compared to empirical formulations of the mass transfer coefficient that are based only on the flow velocity.

In the further course of this contribution, the modeling approaches including their governing equations and computational domains are explained in Chapter 2. The experimental validation of the MSM is presented in Chapter 3. In the Result Section 4, several investigations on different scales are presented. Regarding the MSM, performance calculations are conducted, and the influence of the flow direction within the reconstructed microstructure is explored. Mass transfer coefficient extraction is realized for the reconstructed and generated microstructure, with the former being used to compare the approach with empirical formulations in the literature.

## 2. Electrochemical Model

The following section states the underlying electrochemical and physical phenomena of the different scale models. Both half-cell models are parameterized with the organic aqueous system of 4-OH-TEMPO (henceforth referred to as TEMPO)<sup>[15]</sup> as active material.

The MSM is a multiregion modeling framework considering the electrolyte flow, species, and charge transport in the resolved microstructure of the electrode. The governing equations are directly solved for the solid and fluid regions coupled with a Butler–Volmer-type kinetic boundary condition. The entire calculation is discretized with the finite volume method and implemented in the open-source toolbox OpenFOAM version 7. The simulations were conducted on an HPC system using up to 128 cores with an average simulation time of 24 to 48 h.

The HCSM is a simple homogenized model of an ordinary lab-scale cell considering the transport of diluted species in

porous and nonporous media. The reaction of active species is treated in simplified terms. The modeling framework is implemented in COMSOL Multiphysics software version 5.6, and the simulation time is in the order of a few minutes on a desktop computer.

## 2.1. Micro-Scale Model

The underlying MSM builds up on the 3D model established by Qiu et al.<sup>[16,19]</sup> and is based on the numerical approach by Kespe et al.<sup>[50,51]</sup> It considers the flow of electrolyte, species transport, charge transport through the nonoverlapping solid and liquid phases, and the electrochemical reaction at their interface. The focus lies on a battery half-cell. The electrode and the current collector are resolved, whereas the membrane is considered as a boundary condition. Charge and species conservation are ensured throughout all parts of the computational domain. As mentioned above, the model is parameterized with the 4-OH-TEMPO system. Furthermore, sodium chloride is considered as supporting electrolyte utilizing  $\text{Cl}^-$  as charge carrier.<sup>[15]</sup>

### 2.1.1. Computational Domain

Micro-scale modeling aims at the investigation of the physico-chemical phenomena and transport mechanisms in the porous microstructure. Hence, the pore and fiber space must be resolved due to the equations that are directly linked to the computational grid. Precise information about the fiber geometry is necessary as an input for the simulation. In this contribution, the electrode microstructure is obtained by experimental image reconstruction.<sup>[40]</sup> In addition, an artificial structure made of cylinders is generated for comparison. **Figure 1** shows the reconstructed microstructure (left) and the generated domain (right).

Regarding the reconstructed domain, experimental images of graphite felt (SIGRACELL GFD46, SGL Carbon<sup>[52]</sup>) are obtained via X-ray computed micro-tomography as described in previous work.<sup>[40]</sup> The obtained grid is a subset of the electrode sample and includes an additional current collector plate at  $Z = Z^*$ . The membrane boundary area is located at  $Z = 0$  (not visible). In the default simulation case, the electrolyte flows from the inlet at  $Y = 0$  to the outlet at  $Y = Y^*$ . Modification of the flow

direction is possible in positive and negative Y- and X-directions, respectively. The mean fiber and pore sizes are calculated on the basis of the entire micro-CT data.

The generated domain has the same size as the reconstructed excerpt and consists of comparable properties. With this approach, the domain is faster to generate, has fewer cells, and can therefore be simulated faster. Indeed, the main advantage of the artificial setup of the microstructure is the implementation of solid periodic boundary conditions in the X- and Y-directions. To this end, the same solid-fluid segmentation at opposing boundaries is inescapable. Using an excerpt of the real heterogeneous electrode microstructure, this cannot be ensured. The geometrical information of the reconstructed subset (GFD46) and the generated domain (cyFib) is tabulated in **Table 1**.

### 2.1.2. Fluid Transport

The liquid electrolyte flowing through the porous electrode is assumed as an incompressible Newtonian fluid described by the continuity equation and the Navier–Stokes equation given by<sup>[19]</sup>

$$\nabla \cdot \mathbf{u} = 0 \quad (1)$$

$$\frac{\partial \mathbf{u}}{\partial t} + (\mathbf{u} \cdot \nabla) \mathbf{u} = -\frac{1}{\rho} \nabla p + \nu \nabla^2 \mathbf{u} \quad (2)$$

**Table 1.** Geometrical properties of the reconstructed (GFD46) and generated (cyFib) simulation geometry.

Description	GFD46	cyFib
Half-cell dimensions	78 $\mu\text{m}$ $\times$ 78 $\mu\text{m}$ $\times$ 78 $\mu\text{m}$	
Porosity $\epsilon$	0.914	0.88
Specific surface area	58471 $\text{m}^2 \text{m}^{-3}$	55604 $\text{m}^2 \text{m}^{-3}$
Mean fiber size	14 $\pm$ 1 $\mu\text{m}^{\text{a}}$	10 $\mu\text{m}$
Mean pore size	123 $\pm$ 31 $\mu\text{m}^{\text{a}}$	30 $\mu\text{m}$
Number of computational cells	2.8 $\times$ 10 <sup>6</sup>	1.01 $\times$ 10 <sup>6</sup>
Size of computational cells	0.1 – 2 $\mu\text{m}$	0.3 – 2.5 $\mu\text{m}$

<sup>a)</sup>Obtained from image processing.

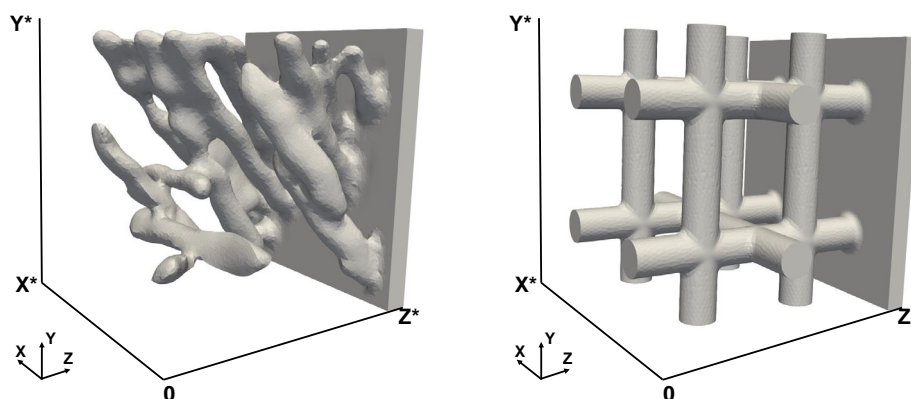


**Figure 1.** Computational domains of the micro-scale model. Reconstructed graphite felt (left) and artificially generated fiber structure (right). Both domains include a current collector plate.

where  $\mathbf{u}$  is the velocity vector,  $t$  is the time,  $\rho$  is the density,  $p$  is the pressure, and  $\nu$  is the kinematic viscosity of the electrolyte. Viscosity and density are constant and uniform throughout the electrolyte. Moreover, the flow is assumed to be laminar and steady state. In the further course of the contribution, the fluid flow is characterized by means of the Reynolds number (Re number)

$$Re = \frac{Ud_f}{\nu} \quad (3)$$

where  $U$  is the magnitude of velocity and  $d_f$  is the fiber diameter. Although the diameter varies in the reconstructed domain, it is set to 10  $\mu\text{m}$  to define the Re number.

### 2.1.3. Species Transport

The concentration of the species within the electrolyte is treated on the basis of the dilute solution theory<sup>[53]</sup> and can change through the following mechanisms: convection due to the velocity field of the electrolyte, diffusion due to a concentration gradient, migration due to a potential gradient, or due to chemical reaction. The model considers the transport of species  $j \in \{\text{TEMPO}, \text{TEMPO}^+, \text{Na}^+, \text{Cl}^-\}$  governed by the convection-diffusion equation<sup>[32]</sup>

$$\frac{\partial C_j}{\partial t} + \nabla \cdot (C_j \mathbf{u}) = \nabla \cdot (D_j \nabla C_j) + \nabla \cdot \left[ \frac{z_j F C_j D_j}{RT} \nabla \phi_e \right] + S_j \quad (4)$$

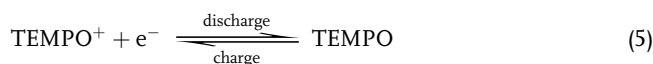
where  $C_j$  is the concentration of species  $j$ ,  $D_j$  is the diffusion coefficient of species  $j$ ,  $z_j$  is the charge of species  $j$ ,  $F$  is the Faraday's constant,  $R$  is the universal gas constant,  $T$  is the absolute temperature,  $\phi_e$  is the electrical potential in the electrolyte, and  $S_j$  is the source term of species  $j$ . Constant diffusivity and no bulk interaction ( $S_j = 0$ ) of the species is assumed throughout the electrolyte. The redox reaction takes place at the electrode–electrolyte interface. The species-dependent transport parameters used throughout this contribution are listed in **Table 2**. Except for chloride, species cross-over through the membrane is neglected, and sodium chloride is completely dissociated into  $\text{Na}^+$  and  $\text{Cl}^-$ .

### 2.1.4. Electrochemical Reaction

The single-electron redox reaction takes place only at the electrode–electrolyte interface and occurs as follows

**Table 2.** Species transport parameters.

Species	Charge ( $z_j$ )	Diffusivity ( $D_j$ )	Ref.
TEMPO	0	$2.95 \times 10^{-9} \text{ m}^2 \text{ s}^{-1}$	[15]
TEMPO <sup>+</sup>	1	$2.95 \times 10^{-9} \text{ m}^2 \text{ s}^{-1}$	[15]
Na <sup>+</sup>	1	$1.33 \times 10^{-9} \text{ m}^2 \text{ s}^{-1}$	[66]
Cl <sup>-</sup>	-1	$2.03 \times 10^{-9} \text{ m}^2 \text{ s}^{-1}$	[66]



The reaction rate of the active species is described by Butler–Volmer-type kinetics. It is the standard electrochemical approach to describe the coupling of the concentration at the active surface and the electrical potential in the solid and liquid phases.<sup>[54]</sup> The reaction rates of TEMPO<sup>+</sup> and TEMPO at the interface are denoted with  $\mathbf{r}_{\text{T}^+}$  and  $\mathbf{r}_{\text{T}}$ , respectively, and during discharge they are<sup>[49]</sup>

$$\begin{aligned} -\mathbf{r}_{\text{T}^+} &= +\mathbf{r}_{\text{T}} \\ &= k(C_{\text{T}}^s)^\alpha (C_{\text{T}^+}^s)^{(1-\alpha)} \left[ \exp\left(\frac{(1-\alpha)F\eta}{RT}\right) - \exp\left(-\frac{\alpha F\eta}{RT}\right) \right] \end{aligned} \quad (6)$$

where  $k$  is the reaction rate constant,  $C_{\text{T}}^s$  and  $C_{\text{T}^+}^s$  denote the concentration of TEMPO and TEMPO<sup>+</sup> at the active surface, and  $\alpha$  is the transfer coefficient. The overpotential  $\eta$  is calculated via

$$\eta = \phi_s - \phi_e - E \quad (7)$$

where  $\phi_s - \phi_e$  represents the local potential difference of electrode and electrolyte and  $E$  is the effective voltage according to the Nernst equation

$$E = E^0 + \frac{RT}{F} \ln\left(\frac{C_{\text{T}^+}^s}{C_{\text{T}}^s}\right) \quad (8)$$

It states the effect of reactant and product surface concentration on the electrode potential. The standard redox potential is  $E^0$ . In addition, the relation between current produced by the reaction and the molar rate is described by Faraday's laws of electrolysis

$$\mathbf{i} = F \mathbf{r} \quad (9)$$

where  $\mathbf{i}$  is the current density.

### 2.1.5. Charge Transport

The conservation of charge holds true within the electrode and the electrolyte. Thus, a divergence-free current density field ensues in both domains

$$\nabla \cdot \mathbf{i} = 0 \quad (10)$$

The governing equation for the potential field  $\phi_s$  in the electrode fibers is represented by Ohm's law

$$\nabla \cdot (\kappa_s \nabla \phi_s) = 0 \quad (11)$$

where  $\kappa_s$  is the electrical conductivity of the electrode.

The potential field in the electrolyte is obtained via

$$\nabla \cdot \left[ \kappa_e \nabla \phi_e + F \sum z_j D_j \nabla C_j \right] = 0 \quad (12)$$

where  $\kappa_e$  is the ionic conductivity and is defined as

$$\kappa_e = \frac{F^2}{RT} \sum_j z_j^2 D_j C_j \quad (13)$$

Nano-scale processes like double-layer formation at the interface are not resolved, and charge neutrality is presumed in the model. The physical properties and operating parameter values are summarized in **Table 3**. The viscosity and density of the electrolyte are assumed to be the same as for NaCl solution due to the low solubility of TEMPO.<sup>[15]</sup> In the further course of this contribution, 1 M and 1.5 M NaCl solutions are used.

### 2.1.6. Boundary and Initial Conditions

**Boundary Conditions for Fluid Transport:** For the fluid flow of electrolyte, no-slip boundary conditions are stated on the fluid–solid interfaces at the electrode, current collector, and membrane. The characteristic average flow velocity is applied as initial condition in the electrolyte domain. The velocity profile at the inlet is mapped from the outlet to avoid inflow effects, whereas a zero-gradient boundary condition is set at the outlet. Regarding the remaining electrolyte boundaries ( $X = 0$  and  $X = X^*$ , compare Figure 1), periodic boundary conditions are imposed. To ensure a pressure gradient that drives the electrolyte flow, the pressure is set to zero at the outlet and a zero-gradient boundary condition is set at the inlet.

**Boundary Conditions for Species Transport:** The model uses either Dirichlet or mapped boundary conditions for the concentration at the inlet. In the former case quasi-steady-state simulations are performed assuming an infinite and constant supply of electrolyte. Using the mapped boundary condition, the outlet concentration is mapped at the inlet and a complete charge or discharge cycle is simulated. Zero-gradient boundary conditions are applied at the outlet. The initial concentrations of the individual species are derived from the regarded electrolyte mixture and the state of charge (SOC)

$$\text{SOC} = \frac{\int C_{\text{TEMPO}^+}(x, t) dV_{\text{el}}}{V_{\text{el}} C_{\text{TEMPO}^+}^{\text{max}}} \quad (14)$$

**Table 3.** Physical properties and operating parameters.

Description	Symbol	Value	Ref.
Electrolyte viscosity (1 M)	$\nu$	$0.9380 \times 10^{-6} \text{ m}^2 \text{ s}^{-1}$	[67]
Electrolyte density (1 M)	$\rho$	$1036 \text{ kg m}^{-3}$	[68]
Electrolyte viscosity (1.5 M)	$\nu$	$0.9675 \times 10^{-6} \text{ m}^2 \text{ s}^{-1}$	[67]
Electrolyte density (1.5 M)	$\rho$	$1055 \text{ kg m}^{-3}$	[68]
Solid electrode conductivity	$\kappa_s$	$200 \text{ S m}^{-1}$	[52]
Operating temperature	$T$	298 K	
Reaction rate constant	$k$	$2.6 \times 10^{-6} \text{ m s}^{-1}$	[15]
Transfer coefficient	$\alpha$	0.5	a)
Standard redox potential	$E^0$	0.8 V	[15]

a) Approximation.

where  $V_{\text{el}}$  is the electrolyte volume and  $C_{\text{TEMPO}^+}^{\text{max}}$  is the individual maximum TEMPO<sup>+</sup> concentration. For the remaining electrolyte boundaries ( $X = 0$  and  $X = X^*$ ), periodic conditions are imposed. The concentration gradient of the chemically active species at the electrolyte–electrode interface is calculated using Equation (12), where the inside of the square brackets is equated with the Butler–Volmer current density. This can be determined with Equation (6) and (9). On account of numerical reasons, the gradient for TEMPO<sup>+</sup> is calculated, whereas the gradient for TEMPO is set as the reverse. For Na<sup>+</sup>, the flux is set to zero at the interface. At the electrolyte–membrane interface, zero-gradient boundary conditions are set for all species. The transport of Cl<sup>−</sup> through the membrane in order to account for charge balancing is treated in simplified terms according to.<sup>[19]</sup> Hence, the depletion and generation of Cl<sup>−</sup> are considered at the active surface to ensure electroneutrality in the bulk.

**Boundary Conditions for Charge Transport:** To ensure current continuity in the solid electrode domain, the potential at the current collector boundary ( $Z = Z^*$ ) is assumed to be uniform and per-iteration fixed at a specific value ( $\phi_{\text{cc}}$ ). Further, the integral electronic current density at the current collector (cc) and the ionic current density at the solid–electrolyte interface (se) must be identical

$$\int \mathbf{n} \cdot i_{\text{s,cc}} dA_{\text{cc}} = - \int \mathbf{n} \cdot i_{\text{s,se}} dA_{\text{se}} \quad (15)$$

The surface unit normal vector pointing outward the relevant domain is  $\mathbf{n}$  and  $A$  is the area. To achieve a certain external charge or discharge current density  $i_{\text{ext}}$ , the potential at the current collector is iteratively adjusted each time step such that<sup>[50,51]</sup>

$$\int \mathbf{n} \cdot i_{\text{s,se}} dA_{\text{se}} = i_{\text{ext}} \cdot A_{\text{mem}} \quad (16)$$

The external current density  $i_{\text{ext}}$  is related to the membrane area  $A_{\text{mem}}$ .<sup>[11]</sup> To fulfill charge conservation between the electrode and the electrolyte, the potential at the electrolyte–solid interface is chosen so that

$$i_{\text{BV}} = \mathbf{n} \cdot i_{\text{se}} = -\mathbf{n} \cdot i_{\text{es}} \quad (17)$$

whereas  $i_{\text{BV}}$  is the Butler–Volmer current density pursuant Equation (6) and (9). Hence, the electric current density  $i_{\text{se}}$  at the interface from the electrode side is equal to the ionic current density  $i_{\text{es}}$  at the electrolyte side of the interface. On the remaining boundaries of the electrolyte and solid domain, periodic conditions are applied to the potential. As we consider only a half-cell, the membrane potential is set to 0 V.

## 2.2. Homogenized Model

The two-dimensional, homogenized, and steady-state cell-scale model (HCSM) considers a flow battery half-cell in though-plane direction. It is parameterized with the physical properties of the aqueous TEMPO-system as well. The electrode properties are identical to the ones obtained for the reconstructed microstructure.

### 2.2.1. Computational Domain

The modeled domain represents a fictional experimental lab-scale cell and is depicted in **Figure 2**. It consists of a primary manifold at the inlet and outlet of the electrode to ensure a homogeneous distribution of electrolyte in the porous electrode. Detailed geometrical data are summarized in **Table 4**. The electrolyte flows through the cell from the bottom right (inlet) to the top left (outlet).

### 2.2.2. Governing Equations

The free flow of the electrolyte in the manifold is governed by Equation (1) and (2). The fluid flow within the porous electrode is described by Darcy's law

$$\mathbf{u} = -\frac{K}{\mu} \nabla p \quad (18)$$

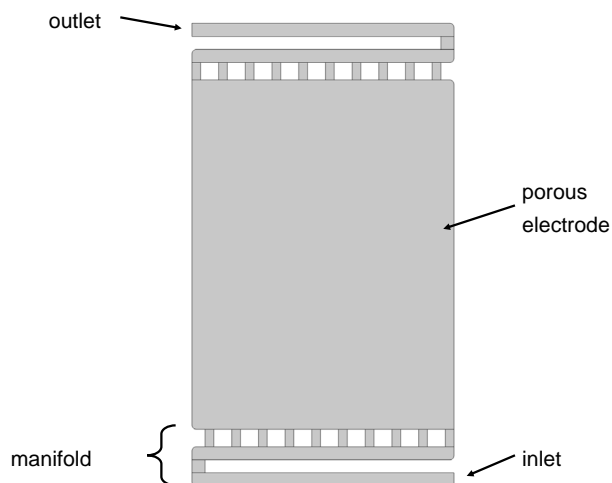


**Figure 2.** Computational domain of the 2D homogenized cell-scale model including inlet and outlet manifold as well as the porous electrode.

**Table 4.** Geometrical properties of the computational domain of the HCSM.

Description	Symbol	Value
Electrode height within the cell	$h_c$	80 mm
Electrode width within the cell	$w_c$	60 mm
Manifold channel width	$w_m$	3 mm
Thickness distributor inlets	$t_i$	2 mm
Height of distributor inlets	$h_i$	4 mm
Number of distributor inlets	$n_i$	10
Height of vertical channel section	$h_{vc}$	3 mm
Gap between the respective inflow channels	$(w_c - w_m - n_i \cdot t_i)/(n_i - 1)$	mm
Radius of fillet	$r_f$	1 mm
Domain depth	$d_d$	4 mm

where  $K$  is the permeability and  $\mu$  is the dynamic viscosity. Using the Carman–Kozeny equation, the permeability can be expressed as<sup>[55]</sup>

$$K = \frac{d_f^2 \varepsilon^3}{180(1 - \varepsilon)^2} \quad (19)$$

where  $\varepsilon$  is the porosity. Although this relation actually describes the flow through packed beds of spherical particles, it can be used for fibrous porous media in flow battery application due to the low Reynolds number and comparatively high porosities.<sup>[56]</sup> The scalar transport of the active species can be described as follows

$$\mathbf{u} \cdot \nabla c = D_c \nabla^2 c + R_c \quad (20)$$

where  $c$  is the concentration,  $D_c$  is the diffusion coefficient, and  $R_c$  is the volumetric reaction rate of the active species. For simplicity, the model accounts for one active species that is transported by the fluid flow and consumed or produced depending on either charge or discharge operation. In actual fact, the above-mentioned convection-diffusion equation possesses an additional migration term which is neglected in the HCSM due to its minor transport effect in through-plane direction.<sup>[22,24]</sup> Concerning the porous medium, an effective diffusivity model is used where the diffusion coefficient is calculated according to the Bruggeman correction<sup>[57]</sup>

$$D_c^{\text{eff}} = \varepsilon^{3/2} D_c \quad (21)$$

where  $D_c^{\text{eff}}$  is the effective diffusion coefficient. The consumption and generation of active species is generally described by Equation (6). This nonlinear relation requires knowledge of the electrical current and overpotential, which are not present in the HCSM. Therefore, a simplified reaction term<sup>[28,29]</sup> is used to express the electrochemical generation of active species

$$R_c = k_m A_V (c_{\text{max}} - c) \quad (22)$$

where  $k_m$  is the mass transfer coefficient,  $A_V$  is the specific active surface area of the porous electrode, and  $c_{\text{max}}$  is the maximal concentration of active material in the electrolyte. The mass transfer coefficient can be written as<sup>[42]</sup>

$$k_m = \beta |\mathbf{u}|^\alpha \quad (23)$$

where  $\beta$  and  $\alpha$  are empirical parameters depending on the electrochemical system and electrode.

## 2.3. Initial and Boundary Conditions

### 2.3.1. Fluid Transport

Pressure and velocity field are initialized with zero. At the inlet, a Dirichlet boundary condition is set for the velocity. The inlet velocity is calculated using a prescribed flow rate. Therefore, the depth of the domain is assumed. At the outlet, a zero-gradient condition is applied. The pressure is fixed to zero at the outlet, and a Neumann condition is set at the inlet.

### 2.3.2. Species Transport

The species  $c$  within the HCSM represents TEMPO which is generated during discharge. For that reason, the initial concentration field and the inlet concentration are set to zero. In the further course, only discharge operation is considered.

## 3. Experimental Validation of the Micro-Scale Model

The MSM is validated against a homogenized and a pore-scale vanadium model in previous work<sup>[40]</sup> due to the absence of experimental TEMPO data. In the context of this contribution, galvanostatic experiments using the TEMPO system are realized for validation. The experiments are conducted with a *redoxme FEC H-Cell*<sup>[58]</sup> containing a cationic membrane and a glassy carbon electrode in contact with graphite felt fitted into the cell compartment. For this validation, methyl-viologen was used in the other compartment. The cell is able to measure half-cell potentials independently. Regarding the operation, the current density is  $2.83 \text{ mA cm}^{-2}$  and the initial concentration is  $0.011 \text{ M TEMPO}$  in  $1 \text{ M NaCl}$ . The velocity is estimated to be  $0.0177 \text{ m s}^{-1}$  corresponding to a flow rate of  $30 \text{ mL min}^{-1}$  used in the experimental cell. To reproduce the experimental data, the reconstructed microstructure is used.

Figure 3 shows the half-cell potential versus SOC for charge (left) and discharge (right) operation. The experimentally obtained potential versus standard hydrogen electrode (SHE) is depicted with a solid red line and corresponds to the first charge and discharge cycle. The initial simulation results are marked in black. To fit the experimental curve, additional  $75 \text{ mV}$  are subtracted for the charge and added for the discharge case, as represented in gray. It should be noted that in the simulations, certain SOC are simulated using the quasi steady-state approach with constant inlet concentration. The experimental curve shows the typical trend originating from the Nernst equation. Regarding discharge, the initial SOC cannot be reached. This originates from self-discharge due to crossover or electrochemical instability of the TEMPO radicals.<sup>[59]</sup> The experiment and the simulation results are in good agreement for charge

and discharge. Especially the shape of the curve in limiting SOC ranges is reproduced well by the model. These limiting ranges relate to high SOC in charge and low SOC in discharge, respectively. In contrast, the opposed regions are not depicted fully congruently. The missing symmetry of the curve originates from using  $\text{TEMPO}^+$  concentration as limiting factor as described in Subsection 2.1.6. To match the potential level of the experimental curve, a fitting voltage parameter of  $75 \text{ mV}$  is applied.<sup>[22,24,60,61]</sup> The discrepancy of the potential arises from the usage of the dilute solution theory, where it is assumed that ions behave ideal and do not interact with each other in the bulk. The validity of this theory is questionable for aqueous organic electrolytes.<sup>[62]</sup> In order to account for the nonidealities of mixing, activity coefficients should be used instead of the concentrations in the Nernst equation (Equation (8)). However, these activities are unknown for the TEMPO system. Concerning low SOC in the charge case, the maximum deviation is 6%. For high SOC in the discharge case, the maximum deviation is 7%.

## 4. Results and Discussion

In the underlying section, the MSM shows predictions of power density under different operating conditions. Further, different flow directions are compared under several operating conditions to make statements about the statistical resilience of the reconstructed microstructure. Moreover, the discharge characteristics of the computational domains are taken into account as well. Subsequently, the mass transfer coefficient is extracted from MSM simulations and implemented into the HCSM using a fitting function. This is followed by a detailed parameter study and a comparison of the presented approach with formulations found in the literature.

### 4.1. Performance Data from the Micro-Scale Model

Capturing the exact morphology of the electrode microstructure, the MSM is capable of giving precise information of the spatial distribution of key parameters and their influence on cell performance. The power density is one of the key factors of flow batteries and is dependent on flow rate, concentration, and

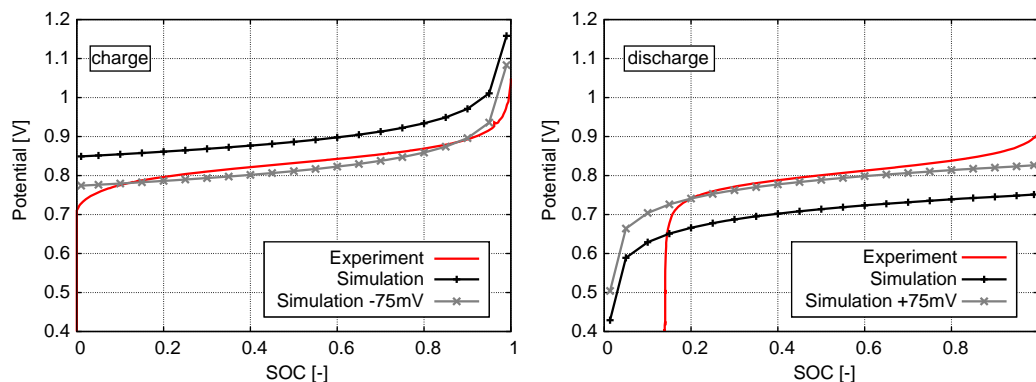


**Figure 3.** Half-cell potential versus SOC for the first charge (left) and first discharge (right) cycle of the *redoxme* cell. The experimental curve is marked in red, whereas the initial simulation result is colored in black. To fit the experiment, the simulated potential is modified with  $75 \text{ mV}$  represented in gray. The current density is  $2.83 \text{ mA cm}^{-2}$  and the concentration is  $0.011 \text{ M TEMPO}$  in  $1 \text{ M NaCl}$ .



current rate. In the following, the power density is investigated under different operating conditions. Simulation studies are performed capturing two different initial concentrations and discharge current densities according to Liu et al.<sup>[15]</sup> The chosen values orientate toward solubility of active material and toward appropriate current density. The concentration is 0.1 M TEMPO in 1 M NaCl and 0.5 M TEMPO in 1.5 M NaCl, whereas the latter represents the solubility limit of TEMPO in NaCl.<sup>[15]</sup> The simulations are performed using constant inlet concentration with SOC of 50%. The galvanostatic discharge current density is 20 and 80 mA cm<sup>-2</sup>. Furthermore, additional 75 mV obtained from the experimental validation are included to calculate the resulting power density. The flow rate ranges correspond to Re numbers of  $5 \times 10^{-4}$ ,  $5 \times 10^{-3}$ , and  $5 \times 10^{-2}$ .

**Figure 4** shows the obtained power density as a function of the Re number for four combinations of the mentioned operating conditions. Regarding low current density, the power density of both concentration levels is of conformable magnitude and stays constant over the range of Re numbers. Different electrolyte velocities do not affect the power density, since sufficient active material is supplied on the surface anyway. The same holds true for the current density of 20 mA cm<sup>-2</sup>. The low current density is provided without significant voltage loss. This means that even the lowest flow rate is adequate to ensure enough active material at the surface.

Regarding high current density of 80 mA cm<sup>-2</sup>, diverse power density levels are reached with different concentrations. The use of higher concentrated electrolyte leads to higher power density due to increased electrolyte conductivity and improved migration at higher concentrations. Additionally, the effect of flow rate on power density becomes distinct. In both cases, the power density decreases with decreasing Re number. The decline is slight for a high concentration of 0.5 M, whereas it is pronounced for a low concentration of 0.1 M. With respect to the latter, mass transfer limitations come to light. Low concentration and low flow rate lead to a distinct voltage loss at high current density. Taken together, the MSM is capable to make statements of the operating conditions and their influence on performance.

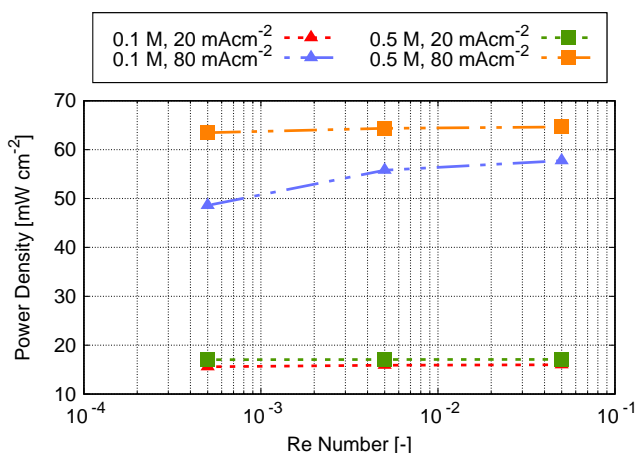


**Figure 4.** Power density over Re number for two different initial concentration levels and discharge current densities. Simulations are performed using a constant inlet concentration with SOC of 50%.

## 4.2. Statistical Resilience of the Reconstructed Microstructure

The reconstructed micro-structure represents the complete electrode only to a certain degree and depends on the chosen area sampled in the XCT. Moreover, the electrode cannot be considered completely homogeneous when it comes to real cell-scale application. Therefore, the microstructure is investigated under different flow directions to gain statistical resilience about its behavior. Furthermore, it is compared to the artificially generated domain which is closer to ideality. Four possible flow directions are examined. In addition to the default positive Y-direction, the negative Y- and negative and positive X-directions are considered. For that purpose, depletion of TEMPO<sup>+</sup> concentration is investigated. Moreover, the discharge behavior in one single flow direction is analyzed using the artificially generated domain as shown in Figure 1. This is due to the symmetric character of the domain.

Steady-state discharge simulations using constant inlet concentrations are performed for all operating parameter combinations introduced in Section 4.1. The initial concentration is 0.1 M TEMPO in 1 M NaCl and 0.5 M TEMPO in 1.5 M NaCl with SOC 50%. The discharge current density is 20 and 80 mA cm<sup>-2</sup>. The Re number of the flow regime is  $5 \times 10^{-4}$ ,  $5 \times 10^{-3}$  and  $5 \times 10^{-2}$ . This results in 60 unique micro-scale simulations that provide a quantitative examination of the reliability of the reconstructed microstructure.

**Figure 5**(left) exemplarily shows the mean TEMPO<sup>+</sup> concentration within the electrolyte region over time during discharge for 0.1 M TEMPO in 1 M NaCl, 80 mA cm<sup>-2</sup>, and Re number  $5 \times 10^{-2}$ . The course of the respective flow directions is highlighted with different colors. After a certain time, the steady-state concentration is reached with respect to all directions. Here, supply and consumption are in equilibrium. Regarding the artificially generated microstructure (cyFib), the equilibrium is reached considerably earlier than for the microstructure. This originates from the fact that the solid fiber domain extends uniformly throughout the simulation domain and is accompanied by lower flow resistance and better mass transport.

The numerous simulations are composed of twelve various operating conditions and five flow directions (including cyFib). For comparison, the respective mean values of the different directions are calculated for each operating condition. Hence, the deviation of every flow direction from the mean value can be determined to show the influence of microstructure under certain conditions.

**Figure 5**(right) shows box plots of the deviation from the mean value for the respective flow directions. The height of the boxes represents the interquartile range, meaning that the middle 50% of deviations are located in this interval. For all flow directions, the box ranges between zero and one and a half percent. This means that the different directions behave similarly for most of the operating conditions. The colored solid line within the box represents the median which divides the data set into two areas, each containing 50%. In every case, the median is below one percent deviation to the mean value enforcing the alike behavior of flow directions. Furthermore, it is mostly located in the lower part of the box originating from the skewness of

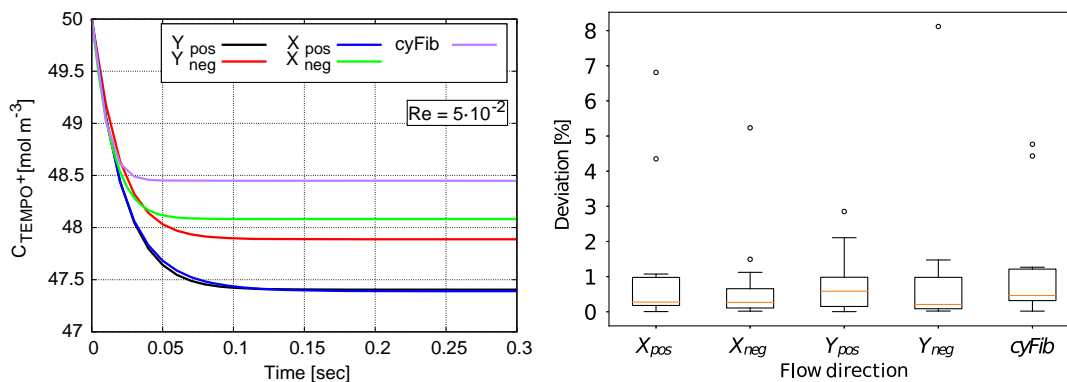


**Figure 5.** (left) Mean TEMPO<sup>+</sup> concentration over time for Re number  $5 \times 10^{-2}$ . The initial concentration is 0.1 M TEMPO in 1 M NaCl, and the discharge current density is  $80 \text{ mA cm}^{-2}$ . Simulations are performed using a constant inlet concentration with SOC of 50%. (right) Boxplot of the deviations from the mean value of all 60 simulations for all flow directions of the reconstructed microstructure and for the artificially generated structure.

the data. The antennas outside the box (whiskers) mark the last data point which is inside the 1.5 times of the interquartile range. However, the boxplot includes outliers that are plotted individually because they differ significantly from the rest of the data set. It turns out that the farthest outliers correspond to the operating condition of 0.1 M TEMPO in 1 M NaCl,  $80 \text{ mA cm}^{-2}$ , and Re number  $5 \times 10^{-4}$ . Here, the resulting steady-state concentrations deviate the most from each other, which leads to comparatively high deviations. This is because the mass transfer here is significantly influenced by the flow field in the electrolyte. In conclusion, the different flow directions play a minor part in appropriate operating conditions. In the underlying study, SOC and velocity are high enough to prevent the significant absence of active material in the domain. Otherwise, when reaching extreme operating conditions, differences become apparent but cannot lead to the determination of a superior flow direction. Moreover, the steady-state mean concentration is chosen for comparison due to simplicity and numerical stability. For future investigations, quantities like surface concentration or the comparison of whole discharge cycles are of interest.

In **Figure 6**, the discharge behavior of the reconstructed and artificially generated microstructure is compared at different Re

numbers. Full discharge is simulated for 0.1 M TEMPO in 1 M NaCl,  $80 \text{ mA cm}^{-2}$ , and Re-Number of  $5 \times 10^{-2}$  (left) and  $5 \times 10^{-4}$  (right). These operating conditions are chosen because they are the ones most likely to result in mass transfer limitations as shown earlier. The graphs show the half-cell potential over SOC including 75 mV potential correction obtained from experimental validation.

Regarding high SOC, the course of potential is comparatively similar for the different domains independent of the Re number. In the further discharge course, differences occur, whereas the artificially generated domain possesses a higher potential at equal SOC. This difference is more pronounced and occurs earlier for the low Re number. For instance, at SOC 40%, the deviation of potential is 1.1% for Re numbers of  $5 \times 10^{-2}$  and 1.6% for  $5 \times 10^{-4}$ . The mass transfer limitation is more pronounced at lower flow rates. All discharge curves end before reaching SOC 0% because the surface concentration falls below zero earlier. The most interesting finding is the relative position of the curves. The artificially generated domain has a slightly minor active surface than the reconstructed domain. Hence, one would expect a lower potential due to higher overpotentials. At equal discharge current density, the actual current at the interface is

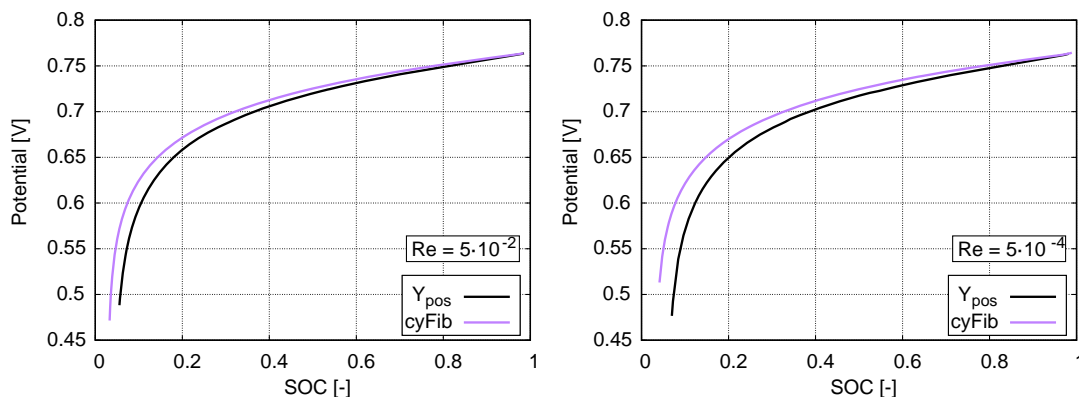


**Figure 6.** Comparison of the reconstructed microstructure (flow in positive Y-direction, Y<sub>pos</sub>) and the structured geometry (cyFib). Half-cell potential versus SOC for Re number  $5 \times 10^{-2}$  (left) and Re number  $5 \times 10^{-4}$  (right). The initial concentration is 0.1 M TEMPO in 1 M NaCl and the discharge current density is  $80 \text{ mA cm}^{-2}$ . Simulations are performed using mapped inlet concentration boundary condition.

higher because of less area. This would result in higher overpotentials that reduce the overall half-cell potential. However, this is not the case in the underlying investigation. The simpler structure and more uniform extension within the simulated volume lead to a better distribution of active material. Dead zones with a lack of active material can thus be avoided.

### 4.3. Extraction of the Mass Transfer Coefficient

According to Lewis and Whitman,<sup>[41]</sup> the mass transfer coefficient is defined in the film theory of mass transfer

$$N_c = k_m A (c_{\text{bulk}} - c_{\text{surf}}) \quad (24)$$

where  $N_c$  is the molar flux of concentration  $c$ ,  $A$  is the active surface area,  $c_{\text{bulk}}$  is the concentration in the bulk electrolyte, and  $c_{\text{surf}}$  is the concentration at the active surface. By dividing by the active area, Equation (24) can be written as

$$k_m = \frac{r}{c_{\text{bulk}} - c_{\text{surf}}} \quad (25)$$

To calculate the mass transfer coefficient, the reaction rate  $r$  is determined by using Faraday's law (Equation (9)) and the applied current density at the interface. Further, bulk and surface concentration must be known. The bulk concentration is assumed to be the average concentration of active material within the electrolyte domain. The surface concentration can be extracted directly due to the nature of the MSM, whereas an average is taken as well. Compared to the similar approach by Kok et al.,<sup>[17]</sup> the determination of  $k_m$  is achieved by using detailed Butler–Volmer-type kinetics, migration, and the specification of the TEMPO system. In fact, mass transfer is dependent on the flow velocity. However, the flow regime in the porous electrode is comparatively uniform which justifies the investigation at constant Re number as done below. Furthermore, the effect of SOC on the mass transfer coefficient is explored.

The HCSM accounts for the generation of a single species up to a maximum concentration. This is why TEMPO concentration is observed in the further course to characterize the mass transfer in particular and the discharge behavior of the flow battery in

general. **Figure 7** (left) shows the extracted mass transfer coefficient according to Equation (25) versus SOC. Graphs for the reconstructed and the generated microstructures are depicted for different Re numbers. The operating conditions are 0.1 M TEMPO in 1 M NaCl and  $80 \text{ mA m}^{-2}$ , whereas mapped boundary conditions are used to simulate a whole discharge process. Comparing the different domains, an enhanced mass transfer can be observed for the generated microstructure due to its isotropic character and an enhanced flow resistance of the reconstructed domain. In either case, the higher the Re number, the higher the  $k_m$ . Regarding Re numbers of  $5 \times 10^{-4}$  and  $5 \times 10^{-3}$ , the graphs are almost congruent. In general, the dependency on velocity is not distinct, which can be a result of the comparatively high discharge rate. With regard to the course of the graphs, the coefficient stays constant within the middle range of SOC and increases to both sides. This is due to a smaller concentration gradient between bulk and surface. At high SOC, almost no TEMPO is present in the system and at low SOC, the majority of active material is already converted into TEMPO. Mass transfer of TEMPO<sup>+</sup> can be imagined to be mirrored at the abscissa.

In **Figure 7** (right), the simulation results of the mass transfer coefficient regarding the reconstructed domain and a corresponding fitting function are shown in more detail. For better visualization, every third data point is depicted. The fitting function consists of five independent parameters and relates to flow velocity and SOC. It is defined as

$$k_m = c + d \cdot U + \frac{b}{\sin(\pi \cdot a \cdot (\text{SOC} + 0.5 \cdot (\frac{1}{a} - 1)))} + e \cdot \text{SOC} \quad (26)$$

where  $U$  is the magnitude of the mean velocity within the electrode, and the SOC is defined to be in the range between zero and one. The parameters are listed in **Table 5**. To create the function, 320 simulation data points are used. The root mean square error between fit and data is  $2.45 \times 10^{-5}$ . Further, it is worth mentioning, that parameter  $a$  within the sinus is constrained to  $a < 0.97$ . Otherwise, the fitting function predicts  $k_m = \infty$  at SOC = 0 and SOC = 1. Finite values at the boundaries are mandatory to

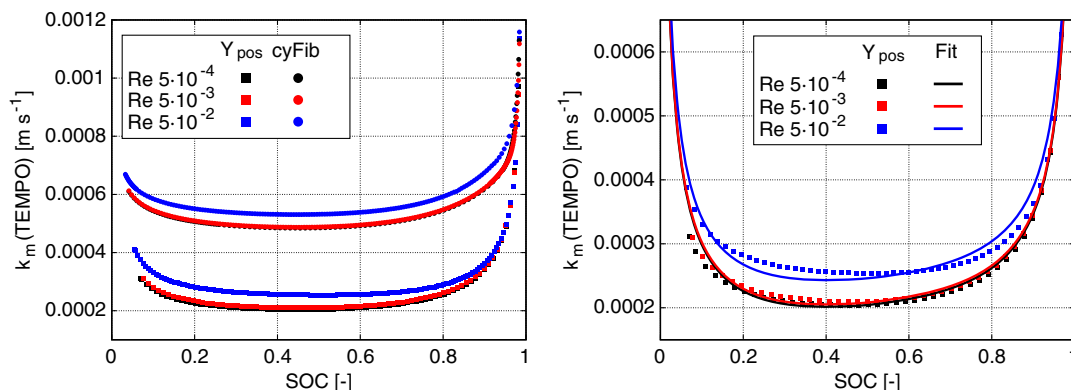


**Figure 7.** (left) Comparison of TEMPO mass transfer coefficient versus SOC for different Re numbers and computational domains. (right) Mass transfer coefficient simulation results and fitting function for the reconstructed domain. The initial concentration is 0.1 M TEMPO in 1 M NaCl and the discharge current density is  $80 \text{ mA cm}^{-2}$ . Simulations are performed using mapped inlet concentration.

**Table 5.** Parameter of the fitting function according to Equation (26).

Parameter	Value	Unit
<i>a</i>	0.9695	–
<i>b</i>	$6.241 \times 10^{-5}$	$\text{m s}^{-1}$
<i>c</i>	$1.114 \times 10^{-4}$	$\text{m s}^{-1}$
<i>d</i>	$8.425 \times 10^{-3}$	–
<i>e</i>	$6.036 \times 10^{-5}$	$\text{m s}^{-1}$

successfully implement the function into the HCSM model as shown hereafter.

#### 4.4. Implementation of the Mass Transfer Coefficient in the Homogenized Cell-Scale Model

In the following HCSM investigation, the extracted fitting function is used to calculate the mass transfer coefficient depending on the local velocity magnitude and SOC in the electrode. Therefore, a parameter study is conducted showing the influence of different flow rates (*Q*) on the beforehand mentioned quantities. The flow rates at the inlet of the manifold correspond to 10, 50, 100, and 150  $\text{mL min}^{-1}$ . All other operating parameters are set to fit the discharge conditions of the mass transfer coefficient extraction in Chapter 4.3. The remaining quantities regarding the HCSM are listed in Table 6.

To evaluate the effect of different flow rates, horizontal and vertical cut lines are defined within the electrode domain. The horizontal line is located shortly above the fifth inlet manifold channel and ends in the middle of the adjacent channels. The vertical line is located in the center of the fifth inlet manifold channel, starts at the transition from channel to electrode, and covers ten percent of the height of the electrode. This is because almost the entire reaction takes place in this section. Table 7 shows the start and end point of the respective lines, whereas the overall spatial origin of the model is located in the center of the HCSM domain.

Figure 8 shows the velocity magnitude, the SOC, and the mass transfer coefficient according to Equation (26) along the dimensionless length of the horizontal and vertical cut lines for the

**Table 6.** Operating conditions of the HCSM.

Description	Symbol	Value
Initial active material concentration	$c_{\text{init}}$	$0 \text{ mol m}^{-3}$
Inlet active material concentration	$c_{\text{inlet}}$	$0 \text{ mol m}^{-3}$
Maximum active material concentration	$c_{\text{max}}$	$100 \text{ mol m}^{-3}$
Inlet velocity	$Q/(w_m \cdot d_d)$	$\text{m s}^{-1}$

**Table 7.** Cut lines within the electrode.

Description	Start	End	Unit
$X^*$ (horizontal)	( $-0.0075 \mid -0.03975$ )	( $0.0045 \mid -0.03975$ )	<i>m</i>
$Y^*$ (vertical)	( $-0.0015 \mid -0.0400$ )	( $-0.0015 \mid -0.0320$ )	<i>m</i>

above-mentioned flow rates. Sub Figure 8a,b show the velocity magnitude. In horizontal direction, the velocity oscillates, showing the maximum above the channels and the minimum in between. For all flow rates, the velocity is near zero above the lands. The local minima above the channels originate from the porous electrode acting as a flow resistance for the free flow in the manifold channels. On impact, part of the flow is directed from the inside to the margins of the channel. This leads to increased velocities at the edges, which affect the first millimeters of the electrode. In vertical direction, the velocity decreases along the cut line, with the decrease being more pronounced at higher flow rates. In general, the velocity decreases in the first five percent of the electrode to a constant value thereafter. Further, the highest velocity detected in the electrode corresponds to a Re number of 0.25. The SOC shows trends similar to those of the velocity for both cut lines. Regarding the horizontal direction (Figure 8c), the SOC is higher above the channels where the fully charged electrolyte enters the electrode. The increments between the different flow rates are nonlinear and arise from reduced mass transfer due to lower velocity. The local minima follow the trend of the velocity as well. It is interesting to note that above the lands, SOC = 0 is reached for each flow rate. This is caused by the comparatively high mass transfer coefficient, especially at the SOC boundaries due to the fitting function. In Chapter 4.5, this phenomenon is discussed in more detail. Further, the SOC decreases in vertical direction because of the discharge process (Figure 8d). The reduction is more pronounced as the flow rate declines and complete discharge is reached within the first 5 percent of the electrode. The trend of the mass transfer coefficient is shown in sub Figure 8e,f. Concerning the horizontal direction, it shows inverse behavior compared to velocity and SOC. Above the channels, fully charged electrolyte is consumed, resulting in different SOC depending on the flow rate. This leads to  $k_m$  values in the data range of the MSM extraction. Additionally, the curves show a similar trend with a local minimum above the center of the channel, except for 10  $\text{mL min}^{-1}$ . This is because here the SOC reaches comparatively low values. Hence, the mass transfer is higher because it reaches the extrapolation zone of the fitting function. Above the lands, the electrolyte approaches SOC = 0 and, consequently,  $k_m$  reaches one of the maximum values originating from the fit. It should be noted here that the maximum can take on other values when using a different fitting function. Furthermore, the lower the flow rate, the wider the maximum plateau above the lands. Less replenishment of active material is transported into the reaction zone due to lower velocities. Along the vertical direction, the U-shaped trend of the  $k_m$  curve (Figure 7, right) can be clearly identified, because the SOC ranges from one to zero. The higher the flow rate, the more pronounced the curve, as more nonconverted electrolyte can penetrate further into the electrode. At the end, SOC = 0 is reached and the effect of different velocities within the electrode becomes visible.

Taken together, the extracted mass transfer coefficient is successfully implemented into the HCSM. However, the reaction zone above the channels is relatively small and in most parts of the cell, no reaction takes place. Hence, the cell is over-designed for the intended system and its chosen operating conditions. Besides, further investigations are required to accurately elucidate the validity of the fitting and the extraction approach in general.

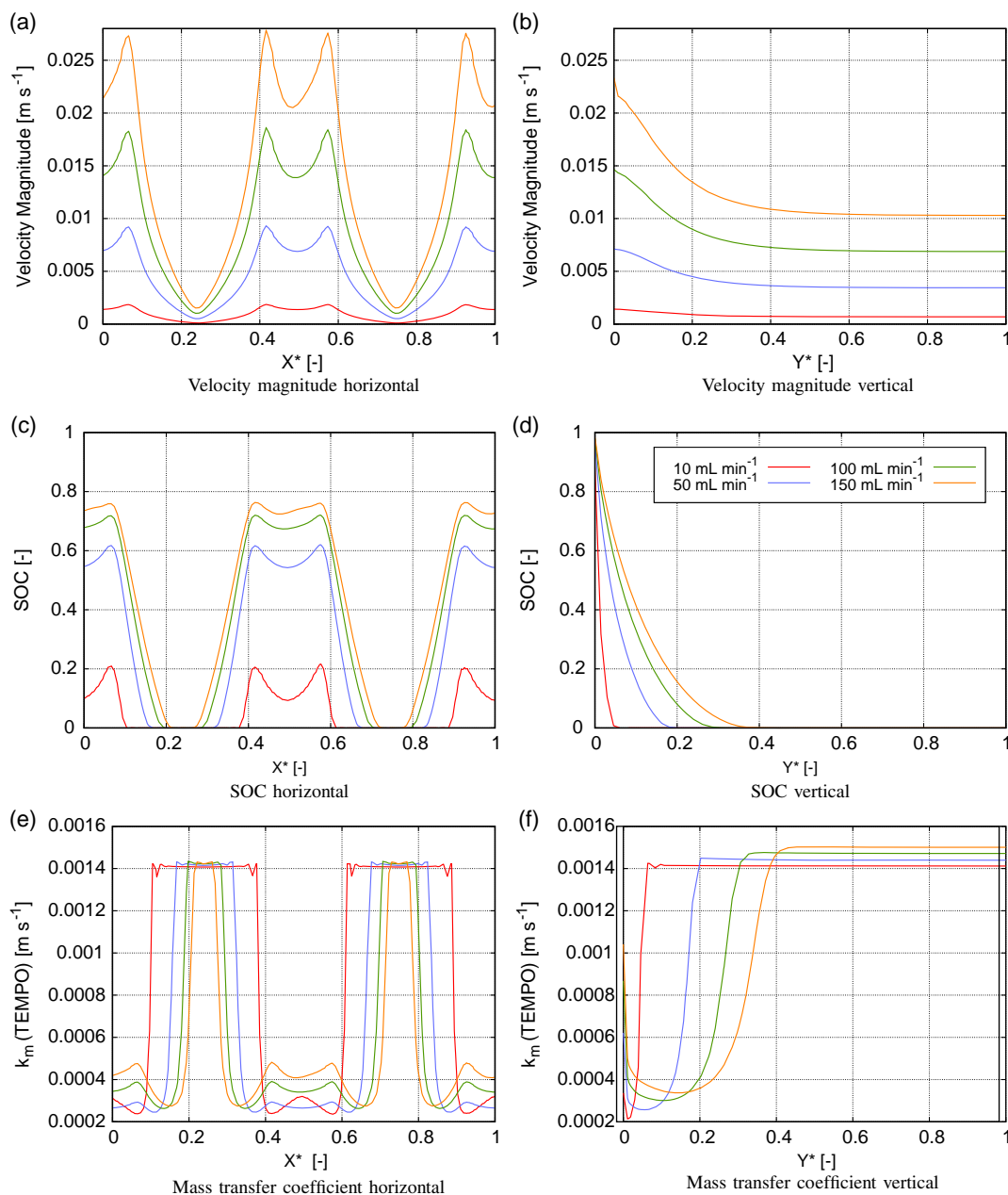


**Figure 8.** Velocity magnitude, SOC, and mass transfer coefficient along the horizontal cut line (left column) and vertical cut line (right column) for different flow rates. The key in (b) holds true for all subfigures. a) Velocity magnitude horizontal; b) Velocity magnitude vertical; c) SOC horizontal; d) SOC vertical; e) Mass transfer coefficient horizontal; f) Mass transfer coefficient vertical.

#### 4.5. Comparison of Mass Transfer Coefficients

In this section, the extracted fit of  $k_m$  is compared to empirical formulations of the correlation between mass transfer coefficient and velocity using the HCSCM as well. The chosen references are based on the work of Schmal et al.<sup>[42]</sup> and Zhang et al.<sup>[18]</sup> The approach by Schmal et al. according to Equation (23) is widely used to describe the mass transfer. Although the experiments are carried out here with potassium hexacyanoferrate, the obtained empirical coefficients  $\beta = 1.6 \times 10^{-4}$  and  $\alpha = 0.4$  are used in (vanadium) flow battery modeling<sup>[22,63–65]</sup> as well as in

this study. In the latter approach by Zhang et al., an empirical correlation is derived from fitting simulated data with experimental results. Here, the TEMPO system and different electrodes are used. The correlation is formulated as

$$k_m = \left( \left( 1 + \exp \left( -4665 \frac{U}{1 \text{ m s}^{-1}} + 42.302 \right) \right)^{-1} + 0.235 \right) \cdot 8.511 \times 10^{-5} \cdot 1 \text{ m s}^{-1}. \quad (27)$$

In both reference approaches, the mass transfer coefficient is solely dependent on the velocity within the electrode. The

comparison is conducted using an inlet flow rate of  $70 \text{ mL min}^{-1}$ . This ensures a flow regime in the electrode corresponding to Re numbers of  $5 \times 10^{-2}$ , where  $k_m$  is extracted from the MSM.

**Figure 9** shows the SOC and the mass transfer coefficient versus the dimensionless length of the horizontal and vertical cut lines presented earlier. Alongside the horizontal cut line (Figure 9a), the SOC fluctuates between channel and land, exhibiting maxima above the channels for all functions. This originates from enhanced velocity and the presence of nonconverted electrolyte in these regions. Regarding the comparative function, the SOC is significantly higher due to the smaller mass transfer coefficient. The two peaks at the maxima above the channels can be also identified in the approach by Zhang et al. Sub Figure 9b shows the vertical direction, where the SOC calculated with the reference functions falls comparatively flat and does not reach zero in the defined range of the cut line. However, in both cases, complete discharge is reached in the first 25 percent of the electrode height. In general, the extracted mass transfer coefficient of the underlying approach is around one order of magnitude higher than the ones predicted by the comparative functions. Along the horizontal cut line, it shows an inverted course (Figure 9c) where the maxima occur above the lands. This can be explained by the significant increase in  $k_m$  in areas with low SOC originated by the fit. Concerning the other curves,  $k_m$  is high above the channels because of the enhanced velocity there. In vertical direction (Figure 9d),

the mass transfer coefficient varies within the first 40 percent of the cut line and remains constant thereafter. The extracted mass transfer coefficient reaches its maximum due to the fit at low SOC, whereas the others reach the minimum due to the decreasing velocity.

In **Figure 10**, excerpts of the inlet manifold and electrode are shown for all three approaches. The domains are colored according to the SOC, calculated with the respective mass transfer coefficients. The electrolyte enters the electrode fully charged and is consumed along the flow. Concerning the approaches by Schmal et al. and Zhang et al., the stepped progression of the reaction can be distinguished. As mentioned earlier, the reaction is completed relatively expeditiously in this approach. In addition, the horizontal and vertical cut lines mentioned earlier are delineated in the central subfigure.

In summary, differences originating from the respective approaches are negligible regarding the comprehensive behavior of the entire cell. The discharge process is completed within the lowest quarter of the cell. It follows that the electrode is too large in vertical flow direction for the applied operating conditions and can be engineered smaller. Clearly, inactive zones can be potential sources of undesirable side reactions. The exact amount of height reduction depends on several operating and system parameters. For instance, reducing the rather high current density would lead in more pronounced reaction zones. Furthermore, the composition of the electrolyte and the active

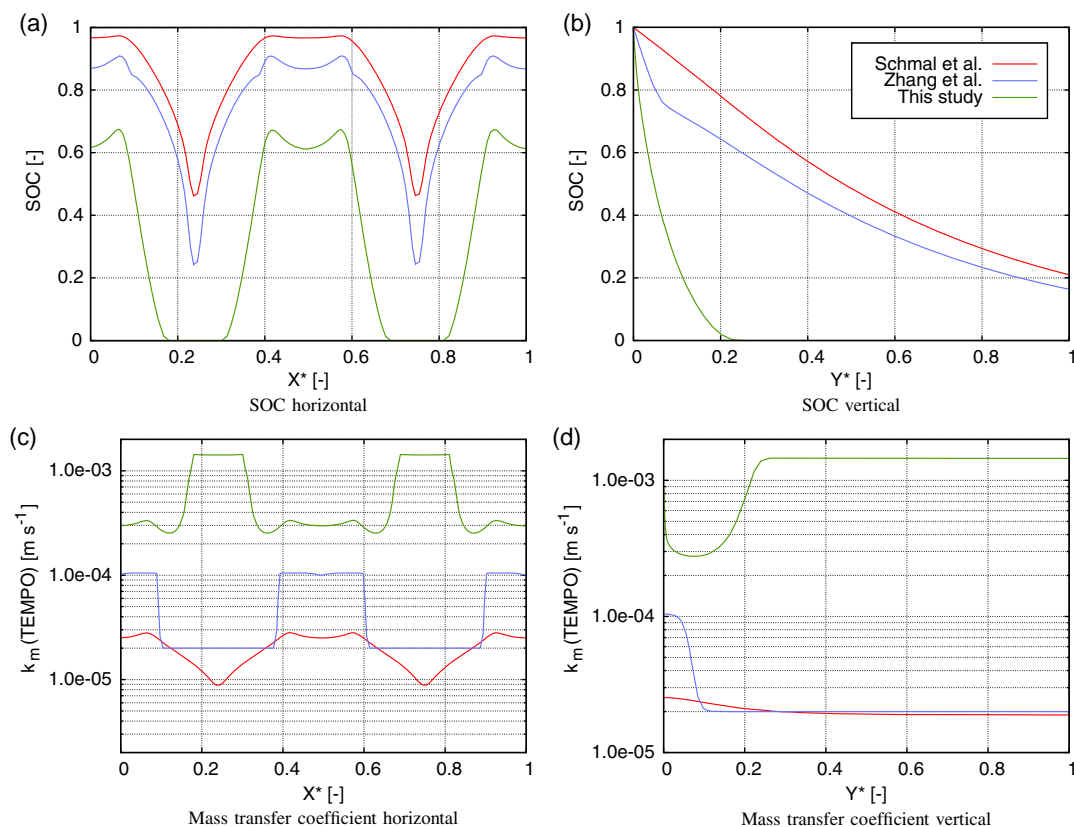


**Figure 9.** SOC (top) and mass transfer coefficient (bottom) along the dimensionless length of the horizontal (left) and vertical cut lines (right) for the empirical formulations of  $k_m$ . The key in (b) holds true for all subfigures. a) SOC horizontal; b) SOC vertical; c) Mass transfer coefficient horizontal; d) Mass transfer coefficient vertical.

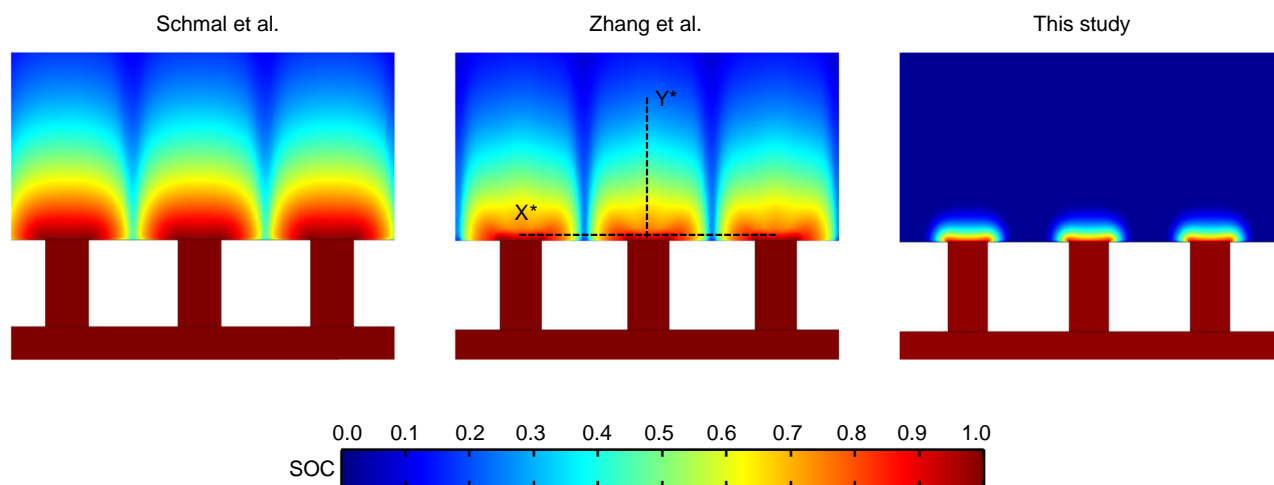


**Figure 10.** Excerpts of the inlet manifold and electrode colored according to the SOC for the respective mass transfer coefficient correlations. Additional representation of the horizontal and vertical cut lines in the central sub-figure.

material concentration play a significant role for creation of the reaction area. In order to determine the optimal height of the electrode, a large parameter study is necessary, but this is beyond the scope of this work. Furthermore, it is worth mentioning that the correlations from the literature are obtained using different porosities of the electrode. This can be considered as reason for the differences as well. Schmal et al. used porosities of 0.83 and 0.96. Zhang et al. considered porosities of 0.8 to 0.85. Besides this, our study shows that the reaction kinetics play a crucial role for designing the cell. The kinetic parameters extracted with our method predict a much faster species conversion in the vicinity of the channels compared to values commonly assumed in the literature. This underlines the urgent need for accurate parameterization of reaction kinetics in redox flow batteries. In addition, full electrochemistry on the homogenized modeling level and experimental investigations are inevitable to extend and proof the numerical results. Taken together, the presented approach is more convincing because it accounts for the micro-structural characteristics of the system and the discharge current density obtained with detailed electrochemistry. Compared to the reference cases, it represents the mass transfer coefficient not only as a function of velocity but also as a function of velocity and SOC.

## 5. Conclusion

In this contribution, a flow battery multiscale simulation approach using the mass transfer coefficient as copula is presented. The half-cell models to be connected are an MSM and a HCSM. To reinforce the reliability of the MSM, validation against experimental data is additionally shown. Spatially resolved micro-scale simulations on reconstructed microstructure are conducted to predict performance characteristics of the flow battery parameterized with the organic TEMPO system under different Re numbers. Therefore, extreme cases regarding the TEMPO solubility and discharge rate are chosen. Further, the reconstructed microstructure is investigated under various flow directions and operating conditions. Moreover, a comparison to an artificially generated domain is drawn. The actual connection

of the two scale models is achieved by the extraction of the mass transfer coefficient from the MSM and its implementation into the HCSM. There, it is studied in a parameter study and compared to empirical formulations of the mass transfer coefficient from the literature.

In general, the MSM fit well to the experimental data, whereas deviations emerge due to taking assumptions in the modeling approach. Moreover, membrane polarization of  $\pm 75$  mV is revealed regarding the model. Further, the use of the concentrated solution theory remains also a subject for future studies with respect to aqueous organic electrolytes.

The findings of the micro-scale investigations are that the Re number has marginal effects on the flow battery performance within the investigated range. Mass transfer limitations and the resulting decrease in power density occur if the operating conditions are chosen in the most unfavorable manner. This is the case for high discharge current density of  $80 \text{ mA cm}^{-2}$  compared with low initial concentration of active material ( $0.1 \text{ M}$ ) and low velocity (Re number  $5 \times 10^{-2}$ ). Regarding these conditions, the flow direction across the reconstructed microstructure has significant impact on the concentration distribution within the electrolyte. In the worst case, a deviation of eight percent from the mean value of all parameter combinations is observed. Moreover, the artificially generated domain is found to achieve a higher half-cell potential than the reconstructed one. Although it possesses a less active surface, the enhanced geometry results in a better supply of active material at the interface and hence a higher potential.

In summary, this article presents a new method for simulative mass transfer determination at the micro-scale. The findings can provide new insights into the use of the mass transfer coefficient, some of which have been vaguely explained. For this purpose, current density and bulk and surface concentration are directly extracted from the MSM. The mass transfer coefficient is consequently calculated at distinct operating conditions and formulated as a function of SOC and velocity. As expected from the previous investigations, it turns out that the mass transfer coefficient of the generated domain is higher than the one obtained

for the microstructure. The key finding is that the extracted mass transfer coefficient including electrochemical information differ greatly from the literature values and predict a much faster species conversion. Additionally, the cell design inspired from existing lab-scale cells is highly oversized for the underlying operating conditions and should be engineered smaller.

For future work, it is inevitable to consider a larger, simulation-based parameter variation for the determination of  $k_m$ . Initial concentration level, current rate, and the computational domain characteristics in general would be additional options for this. Variation of the porosity is also conceivable. As a final remark, it is also vital to mention that the use of the extracted mass transfer coefficient in a HCSM including electrochemical kinetics would lead to a better understanding.

## Acknowledgements

The authors gratefully acknowledge the financial support for this work by the European Union's Horizon 2020 Research and Innovation Programme under Grant Agreement no. 875489. The authors would like to thank Assoc. Prof. Ern. William C. Rose from the University of Delaware for the fruitful discussion about data fitting. The authors also thank Felix Gerbig, Anshuman Chauhan, and Susanne Kespe from the Karlsruhe Institute of Technology for the many fruitful discussions.

Open Access funding enabled and organized by Projekt DEAL.

## Conflict of Interest

The authors declare no conflict of interest.

## Data Availability Statement

The data that support the findings of this study are available from the corresponding author upon reasonable request.

## Keywords

electrode microstructure, experimental validation, flow batteries, homogenized cell-scale modeling, mass transfer coefficient, micro-scale modeling, multiscale approach

Received: February 20, 2023

Revised: March 16, 2023

Published online:

- [1] S. Chu, Y. Cui, N. Liu, *Nat. Mater.* **2017**, *16*, 16.  
 [2] J. Noack, N. Roznyatovskaya, T. Herr, P. Fischer, *Angew. Chem., Int. Ed.* **2015**, *54*, 9776.  
 [3] M. Park, J. Ryu, W. Wang, J. Cho, *Nat. Rev. Mater.* **2016**, *2*, 16080.  
 [4] A. Poullikkas, *Renewable Sustainable Energy Rev.* **2013**, *27*, 778.  
 [5] W. Wang, Q. Luo, B. Li, X. Wei, L. Li, Z. Yang, *Adv. Funct. Mater.* **2013**, *23*, 970.  
 [6] S. Kim, E. Thomsen, G. Xia, Z. Nie, J. Bao, K. Recknagle, W. Wang, V. Viswanathan, Q. Luo, X. Wei, A. Crawford, G. Coffey, G. Maupin, V. Sprenkle, *J. Power Sources* **2013**, *237*, 300.  
 [7] E. Sánchez-Díez, E. Ventosa, M. Guarnieri, A. Trovò, C. Flox, R. Marcilla, F. Soavi, P. Mazur, E. Aranzabe, R. Ferret, *J. Power Sources* **2021**, *481*, 228804.  
 [8] Y. Zeng, T. Zhao, L. An, X. Zhou, L. Wei, *J. Power Sources* **2015**, *300*, 438.  
 [9] Z. Huang, A. Mu, L. Wu, B. Yang, Y. Qian, J. Wang, *ACS Sustainable Chem. Eng.* **2022**, *10*, 7786.  
 [10] B. Khaki, P. Das, *Electrochim. Acta* **2022**, *405*, 139842.  
 [11] J. Winsberg, T. Hagemann, T. Janoschka, M. D. Hager, U. S. Schubert, *Angew. Chem., Int. Ed.* **2017**, *56*, 686.  
 [12] G. J. Simandl, S. Paradis, *Appl. Earth Sci.* **2022**, *131*, 218.  
 [13] J. Asenjo-Pascual, I. Salmeron-Sanchez, J. R. Avilés-Moreno, P. Mauleón, P. Mazur, P. Ocón, *Batteries* **2022**, *8*, 10.  
 [14] J. Chai, A. Lashgari, J. Jiang, *Electroactive Materials For Next-Generation Redox Flow Batteries: From Inorganic to Organic*, American Chemical Society, Washington, DC, USA **2020**, ch. 1, pp. 1–47.  
 [15] T. Liu, X. Wei, Z. Nie, V. Sprenkle, W. Wang, *Adv. Mater.* **2016**, *6*, 1501449.  
 [16] G. Qiu, C. Dennison, K. Knehr, E. Kumbur, Y. Sun, *J. Power Sources* **2012**, *219*, 223.  
 [17] M. D. Kok, R. Jervis, T. G. Tranter, M. A. Sadeghi, D. J. Brett, P. R. Shearing, J. T. Gostick, *Chem. Eng. Sci.* **2019**, *196*, 104.  
 [18] D. Zhang, A. Forner-Cuenca, O. O. Taiwo, V. Yufit, F. R. Brushett, N. P. Brandon, S. Gu, Q. Cai, *J. Power Sources* **2020**, *447*, 227249.  
 [19] G. Qiu, A. S. Joshi, C. Dennison, K. Knehr, E. Kumbur, Y. Sun, *Electrochim. Acta* **2012**, *64*, 46.  
 [20] D. Zhang, Q. Cai, O. O. Taiwo, V. Yufit, N. P. Brandon, S. Gu, *Electrochim. Acta* **2018**, *283*, 1806.  
 [21] L. Chen, Y. He, W.-Q. Tao, P. Zelenay, R. Mukundan, Q. Kang, *Electrochim. Acta* **2017**, *248*, 425.  
 [22] D. You, H. Zhang, J. Chen, *Electrochim. Acta* **2009**, *54*, 6827.  
 [23] A. Shah, M. Watt-Smith, F. Walsh, *Electrochim. Acta* **2008**, *53*, 8087.  
 [24] A. A. Shah, R. Tangirala, R. Singh, R. G. A. Wills, F. C. Walsh, *J. Electrochem. Soc.* **2011**, *158*, A671.  
 [25] H. Al-Fetlawi, A. Shah, F. Walsh, *Electrochim. Acta* **2010**, *55*, 3192.  
 [26] M. Vynnycky, *Energy* **2011**, *36*, 2242.  
 [27] E. Prumbohm, G. D. Wehinger, *Chem. Ing. Tech.* **2019**, *91*, 900.  
 [28] Q. Xu, T. Zhao, *Phys. Chem. Chem. Phys.* **2013**, *15*, 10841.  
 [29] K. Yaji, S. Yamasaki, S. Tsushima, T. Suzuki, K. Fujita, *Struct. Multidiscip. Optim.* **2018**, *57*, 535.  
 [30] K. Yaji, T. Yamada, S. Kubo, K. Izui, S. Nishiwaki, *Int. J. Heat Mass Transfer* **2015**, *81*, 878.  
 [31] F. Wandschneider, D. Finke, S. Grosjean, P. Fischer, K. Pinkwart, J. Tübke, H. Nirschl, *J. Power Sources* **2014**, *272*, 436.  
 [32] E. M. Ryan, P. P. Mukherjee, *Prog. Energy Combust. Sci.* **2019**, *71*, 118.  
 [33] B. K. Chakrabarti, E. Kalamaras, A. K. Singh, A. Bertei, J. Rubio-Garcia, V. Yufit, K. M. Tenny, B. Wu, F. Tariq, Y. S. Hajimolana, N. P. Brandon, C. T. John Low, E. P. L. Roberts, Y.-M. Chiang, F. R. Brushett, *Sustainable Energy Fuels* **2020**, *4*, 5433.  
 [34] O. C. Esan, X. Shi, Z. Pan, X. Huo, L. An, T. Zhao, *Adv. Mater.* **2020**, *10*, 2000758.  
 [35] Q. Zheng, X. Li, Y. Cheng, G. Ning, F. Xing, H. Zhang, *Appl. Energy* **2014**, *132*, 254.  
 [36] D. Zhang, A. Bertei, F. Tariq, N. Brandon, Q. Cai, *Prog. Energy* **2019**, *1*, 012003.  
 [37] A. A. Franco, A. Rucci, D. Brandell, C. Frayret, M. Gaberscek, P. Jankowski, P. Johansson, *Chem. Rev.* **2019**, *119*, 4569.  
 [38] J. Bao, V. Murugesan, C. J. Kamp, Y. Shao, L. Yan, W. Wang, *Adv. Theor. Simul.* **2020**, *3*, 1900167.  
 [39] H. Tao, G. Chen, C. Lian, H. Liu, M.-O. Coppens, *AIChE J.* **2022**, *68*, e17571.  
 [40] A. Wolf, S. Kespe, H. Nirschl, *Pore-Scale Modeling of Flow Batteries*, John Wiley & Sons, Ltd., Hoboken NJ **2023**, ch. 18, pp. 413–442, ISBN 9783527832767.  
 [41] W. K. Lewis, W. G. Whitman, *Ind. Eng. Chem.* **1924**, *16*, 1215.



- [42] D. Schmal, J. Van Erkel, P. J. Van Duin, *J. Appl. Electrochem.* **1986**, 16, 422.
- [43] A. Storck, P. Robertson, N. Ibl, *Electrochim. Acta* **1979**, 24, 373.
- [44] P. S. Fedkiw, J. Newman, *Int. J. Heat Mass Transfer* **1982**, 25, 935.
- [45] P. W. Appel, J. Newman, *AIChE J.* **1976**, 22, 979.
- [46] K. Kinoshita, S. C. Leach, *J. Electrochem. Soc.* **1982**, 129, 1993.
- [47] X. You, Q. Ye, P. Cheng, *J. Electrochem. Soc.* **2017**, 164, E3386.
- [48] J. D. Milshtein, K. M. Tenny, J. L. Barton, J. Drake, R. M. Darling, F. R. Brushett, *J. Electrochem. Soc.* **2017**, 164, E3265.
- [49] S. K. Murthy, A. K. Sharma, C. Choo, E. Birgersson, *J. Electrochem. Soc.* **2018**, 165, A1746.
- [50] M. Kespe, H. Nirschl, *Int. J. Energy Res.* **2015**, 39, 2062.
- [51] M. Kespe, M. Gleiß, S. Hammerich, H. Nirschl, *Int. J. Energy Res.* **2017**, 41, 2282.
- [52] SIGRACELL Battery Felts Datasheet, **2019**, <https://www.sglcarbon.com/pdf/SGL-Datasheet-SIGRACELL-Battery-Felts-EN.pdf> (accessed: February 2023).
- [53] J. Newman, *Electrochemical Systems*, The Electrochemical Society Series, 4th ed., Wiley, Hoboken, NJ **2021**.
- [54] M. Z. Bazant, *Acc. Chem. Res.* **2013**, 46, 1144.
- [55] J. Bear, *Dynamics of Fluids in Porous Media*, Number Parts 1-2 in Dynamics of Fluids in Porous Media, American Elsevier Publishing Company, New York, USA **1972**.
- [56] K. Yazdchi, S. Srivastava, S. Luding, **2011**.
- [57] M. W. Verbrugge, R. F. Hill, *J. Electrochem. Soc.* **1990**, 137, 886.
- [58] redoxme FEC H-Cell 2x1.5ML - Flow Electrochemical H-Cell, **2022**, <https://redox.me/collections/all/products/fec-h-cell-2x1-5-ml-flow-electrochemical-h-cell> (accessed: February 2023).
- [59] W. Zhou, W. Liu, M. Qin, Z. Chen, J. Xu, J. Cao, J. Li, *RSC Adv.* **2020**, 10, 21839.
- [60] K. Knehr, E. Kumbur, *Electrochem. Commun.* **2011**, 13, 342.
- [61] N. Hayer, M. Kohns, *J. Electrochem. Soc.* **2020**, 167, 110516.
- [62] G. Mourouga, D. Chery, E. Baudrin, H. Randriamahazaka, T. J. Schmidt, J. O. Schumacher, *iScience* **2022**, 25, 104901.
- [63] X. Ma, H. Zhang, F. Xing, *Electrochim. Acta* **2011**, 58, 238.
- [64] I. M. Bayanov, R. Vanhaelst, *J. Math. Chem.* **2011**, 49, 1572.
- [65] Q. Zheng, H. Zhang, F. Xing, X. Ma, X. Li, G. Ning, *Appl. Energy* **2014**, 113, 1675.
- [66] N. R. Council, *International Critical Tables of Numerical Data, Physics, Chemistry and Technology*, The National Academies Press, Washington, DC, **1930**.
- [67] J. Kestin, H. E. Khalifa, R. J. Correia, *J. Phys. Chem. Ref. Data* **1981**, 10, 71.
- [68] R. W. Potter, D. L. Brown, U.S. Geological Survey **1975**, pp. 75–636.